buildings

MDPI

Article

A New Continuous Strength Method for Prediction of Strain-Hardening Performance of High-Strength Aluminum Alloy Cylindrical Columns

Lihui Chen [1], Weikai Xu [1], Yusong Chen [1] and Weipeng Sun [2,*]

[1] School of Civil Engineering and Architecture, Suqian University, Suqian 223800, China; chenlh7982@squ.edu.cn (L.C.); wkxu@squ.edu.cn (W.X.); chenys@squ.edu.cn (Y.C.)
[2] School of Mathematics, Jilin University, Changchun 130012, China
* Correspondence: sunwp@jlu.edu.cn

Abstract: This paper aims to develop a new continuous strength method (CSM) to more accurately predict the strain-hardening characteristics of high-strength aluminum alloy circular hollow sections (CHSs) under axial compression. A total of 11 stub column specimens made of 7A04-T6 and 6061-T6 aluminum alloys underwent testing. Additionally, 16 sets of experiment data were gathered from open sources, encompassing various aluminum alloy types such as 6082-T6, 6061-T6, and 6063-T5. Validated by experimental result, the finite element (FE) model was applied in a series of comprehensive parameter studies, supplementing the limited test result of high-strength aluminum alloy stub columns. Based on the experiment and FE results, this paper proposes a new CSM relation to determine the cross-sectional resistance of high-strength non-slender CHS aluminum alloys under compression. The cross-sectional resistance obtained from tests are compared with predicted strengths determined using the European code, as well as the solution of the CSM proposed in a previous study and in this paper. The comparison illustrates that the strength predictions in the European code and the previous study are conservative. Compared with the European code and the previous study, the strength prediction formula proposed in this paper improves accuracy by 11% and 5%, respectively, while reducing scatter by 8.4% and 2%, respectively.

Keywords: axial compression; cross-sectional resistance; high-strength aluminum alloy; strain hardening; continuous strength method

Citation: Chen, L.; Xu, W.; Chen, Y.; Sun, W. A New Continuous Strength Method for Prediction of Strain-Hardening Performance of High-Strength Aluminum Alloy Cylindrical Columns. *Buildings* **2024**, *14*, 3055. https://doi.org/10.3390/buildings14103055

Academic Editor: Hiroshi Tagawa

Received: 22 August 2024
Revised: 22 September 2024
Accepted: 23 September 2024
Published: 25 September 2024

1. Introduction

Steel structures are extensively used in the constructions of buildings and bridges owing to their high strength, excellent plasticity and toughness, as well as the convenience for industrialized production and mechanized, automated construction. Nevertheless, the poor corrosion resistance of commonly used ordinary carbon steel poses significant challenges in humid and corrosive environments, thus leading to serious corrosion issues and maintenance requirements [1]. This not only escalates maintenance expenses but also poses safety risks. Substituting ordinary carbon steel with corrosion-resistant materials emerges as a fundamental solution to these problems. Aluminum alloys present superior appearance, corrosion resistance, and durability compared to ordinary carbon steel, while also offering the advantages of being lighter in weight and possessing a higher strength-to-weight ratio than stainless steel [2,3]. Furthermore, aluminum alloys are 100% recyclable, thereby further reducing carbon dioxide emissions and aligning with the principles of sustainable development [3]. From environmental and economic standpoints, aluminum alloy structures are able to yield better outcomes. Consequently, aluminum alloy structures exhibit extensive prospects for engineering applications. In recent years, increasingly more aluminum alloy load-bearing members have been used in buildings and bridge constructions due to their continual enhancements in mechanical properties. The study of the strength, ductility, and energy dissipation capacity [4,5] of structures is of great importance. This paper focuses on predicting the strength of aluminum alloy structures subjected to monotonic loading.

Circular hollow sections (CHSs) are favored by designers owing to their aesthetics and exceptional structural performance [6]. Most CHSs are thin-walled members, hence local buckling is the main factor affecting their cross-section resistance, whether before or after yield. There are many international design specifications for aluminum alloy structures [7–10]. European code EC9 [8] adopts the cross-section classification method to implicitly treat the local buckling phenomenon. The cross-sections are categorized into four classes based on their sensitivity to local buckling. For compression, yielding for classes 1, 2, and 3 (i.e., non-slender cross-sections) occurs without failing due to local buckling, while local buckling for class 4 (i.e., slender cross-sections) occurs within the elastic range. The stress-strain response of aluminum alloys is strongly nonlinear, with no yield plateau and significant strain hardening. It is different from steel (the stress-strain curve for steel is derived from Reference [11]) as illustrated in Figure 1. Due to strain hardening characteristics of aluminum alloys, the resistance of non-slender cross-sections can be greater than its yield load, which is equal to the cross-sectional area multiplied by the yield stress. Nevertheless, EC9 assumes aluminum alloys to behave as elastic-perfectly plastic materials, thereby limiting the resistance of non-slender cross-sections to the yield load, which proves uneconomical for such sections.

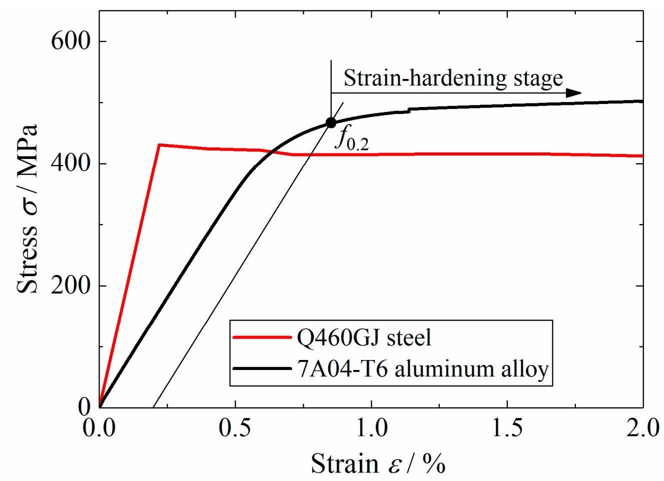

Figure 1. Comparison of stress-strain curves of aluminum alloy and steel.

The continuous strength method (CSM) is a deformation-based structural design approach that allows for rational exploitation of strain hardening [12]. This method was first proposed by Gardner and Nethercot [13] and applied to the hollow section of stainless steel. Compared with the traditional design method, prediction accuracy of the cross-sectional resistance in compression proposed by Gardner improved by about 20%. Subsequently, Ashraf et al. [14] extended this method to other typical sections of stainless steel. In 2008, Gardner [15] formally proposed CSM to predict the cross-sectional resistance of members composed of highly non-linear and strain hardening materials. Over the past decade, CSM was widely extended to the design of steel [16–19], stainless steel [20–23], and aluminum alloy [24–29]. The aforementioned research works mainly focus on the cross-sectional design of members composed of flat plates, such as I-sections, square hollow sections (SHSs), and rectangular hollow sections (RHSs). The cross-sectional resistance of high-strength steel hollow sections under axial compression and bending based on CSM was investigated by Lan et al. [30,31], including circular hollow sections (CHSs), elliptic hollow sections (EHSs), etc. Zhao et al. [32,33] focused on the structural performance of stainless steel CHSs under combined loading. Based on a total of 342 stub columns and bending test results, including high-strength steel, stainless steel and normal strength aluminum alloy, Buchanan et al. [34] proposed the resistance prediction formulas for CHSs. However, the applicability of these formulas mentioned above should be rediscussed when they are used to predict the cross-sectional bearing capacity of high-strength aluminum alloys.

This paper focuses on more accurate prediction of the strain-hardening benefits of high-strength aluminum alloy CHSs under axial compression. As is well known, slender cross-sections have no significant benefit from strain hardening due to local buckling below the yield point. The strain-hardening benefits are only useful in non-slender cross-sections. Considering strain hardening, the resistance of a non-slender cross-section is predicted with the CSM in this paper. Nonlinear finite-element (FE) models are established and validated by comparing with axial compression test results of 7A04-T6 and 6061-T6 aluminum alloy CHS stub column specimens. Subsequently, extensive parametric analysis is conducted using the validated FE models. According to experiments and FE solutions, a regularized cross-section limit is recommended, and a general relation for predicting the bearing capacity of high-strength aluminum alloy non-slender CHSs under axial compression is proposed and established based on the CSM.

2. Experimental Investigation

2.1. Test Specimens

A total of 11 CHS stub column specimens were designed for the axial compression experiment. The specimens were fabricated by using 7A04-T6 and 6061-T6 aluminum alloy, both manufactured in China. The length of each stub column specimens is three times its outer diameter. Details of the geometric dimensions of the specimens are listed in Table 1, where the specimens are labeled to facilitate identification of the specimen type, aluminum alloy grade, and cross-sectional geometry. For example, "SC-7X-86-8.6-A" defines the following specimen. The first part of the label indicates the specimen type, where "SC" refers to the stub column with circular hollow sections; the second part indicates the aluminum alloy grade, where "7X" refers to the high-strength aluminum alloy 7A04-T6; the next part of the label "86" indicates that the outer diameter of the specimen is 86 mm, and "8.6" indicates that the thickness of the specimen is 8.6 mm; and lastly, the letter "A" indicates the first tested specimen among the repeated tests.

Table 1. Geometric dimensions of specimens.

No.	Specimen	Outer Diameter D/mm	Thickness t/mm	Length L/mm	Aluminum Alloy Grade
1	SC-7X-86-8.6-A	86	8.6	258	7A04-T6
2	SC-7X-86-8.6-B	86	8.6	258	
3	SC-6X-50-1.5-A	50	1.5	150	6061-T6
4	SC-6X-50-1.5-B	50	1.5	150	
5	SC-6X-50-1.5-C	50	1.5	150	
6	SC-6X-50-3-A	50	3	150	
7	SC-6X-50-3-B	50	3	150	
8	SC-6X-50-3-C	50	3	150	
9	SC-6X-50-4-A	50	4	150	
10	SC-6X-50-4-B	50	4	150	
11	SC-6X-50-4-C	50	4	150	

2.2. Material Properties

The material properties of 7A04-T6 aluminum alloy were determined through tensile coupon tests. Four tensile coupons were extracted from the curved faces of the CHS stub column in the longitudinal direction. In accordance with the Chinese standard [35], the dimensions of the coupon are illustrated in Figure 2. The tensile coupon test was conducted using a SCHENCK RBO400 hydraulic universal testing machine, equipped with an MFA2 extensometer (Figure 3). The material properties of 7A04-T6 aluminum alloy are presented in Table 2, which includes the Young's modulus (E), nominal yield strength ($f_{0.2}$), ultimate strength (f_u), ultimate strain at ultimate stress (ε_u), based on a gauge length of 50 mm, and strain-hardening exponent (n). It is noteworthy that n is determined through nonlinear regression using the Levenberg–Marquardt optimization algorithm, based on the measured stress-strain data and the following Ramberg–Osgood expression

$$\varepsilon = \frac{\sigma}{E} + K\left(\frac{\sigma}{\sigma_0}\right)^n, \quad (1)$$

where ε is the axial strain, σ is the axial stress, and σ_0 is the axial yield strength. For materials with no obvious yield point such as aluminum alloys, the 0.2% proof stress $f_{0.2}$ is usually taken as the yield strength. K is the material constant, and aluminum alloys take $K = 0.002$.

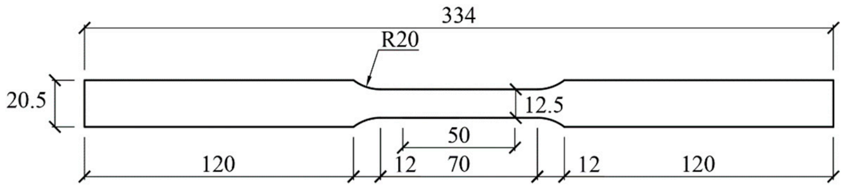

Figure 2. Tensile coupon size of 7A04-T6 aluminum alloy.

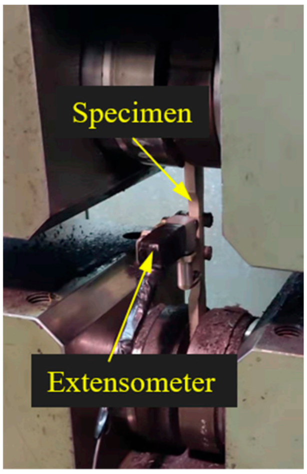

Figure 3. Schematic diagram of the tensile coupon testing device.

Table 2. Material properties of 7A04-T6 aluminum alloy obtained from tensile coupon tests.

Specimen	E/GPa	$f_{0.2}$/MPa	f_u/MPa	ε_u/%	n
7A04-1	72.539	465	574	10	19.2
7A04-2	72.939	461	557	8.0	20.1
7A04-3	71.266	468	547	7.0	23.4
7A04-4	70.838	468	570	9.5	20.4
Mean	71.896	465.5	562	8.6	20.8

The material properties of 6061-T6 aluminum alloy are obtained via stub column tests. The measured material properties obtained from stub column tests of 6061-T6 aluminum alloy CHSs are shown in Table 3, which includes the Young's modulus (E), nominal yield strength ($f_{0.2}$), ultimate strength (f_u), and strain-hardening exponent (n). The data of specimen SC-6X-50-1.5-C are invalid due to abnormal test results. The stress-strain curves of all specimens are shown in Figure 4.

Table 3. Material properties of 6061-T6 aluminum alloy obtained from stub column tests.

Specimen	E/GPa	$f_{0.2}$/MPa	f_u/MPa	n
SC-6X-50-4-A	59.848	250	308	15.7
SC-6X-50-4-B	59.561	253	305	19.1
SC-6X-50-4-C	57.275	255	306	20.9
Mean	58.895	253	306	18.6
SC-6X-50-3-A	68.954	250	281	21.2
SC-6X-50-3-B	62.469	254	285	18.9
SC-6X-50-3-C	61.000	249	282	22.5
Mean	64.141	251	283	20.8
SC-6X-50-1.5-A	63.668	220	230	23.6
SC-6X-50-1.5-B	60.944	224	233	27.5
SC-6X-50-1.5-C	-	-		-
Mean	62.306	222	232	25.6

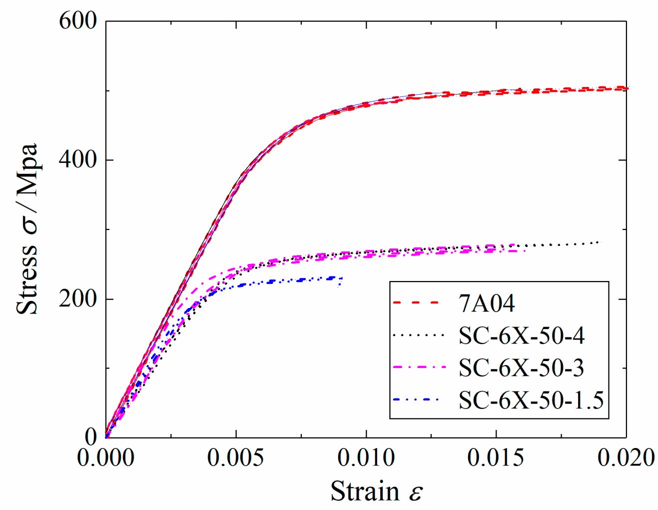

Figure 4. Stress-strain curves of all specimens.

2.3. Stub Column Testing Procedure

Typical stub column tests are shown in Figure 5. The YAW 2000-kN electro-hydraulic servo testing machine was used to apply an axial compressive load to the stub column specimens. The specimens were tested with both ends fixed. Loading of the specimens was controlled via displacement at a constant speed of 0.2 mm/min. The axial load (P) and end shortening (δ) were recorded by the testing machine throughout the loading process. Additionally, four strain gauges were mounted at the mid-span of each specimen, and the data of the mid-span strain were regularly recorded by the static strain test analysis system.

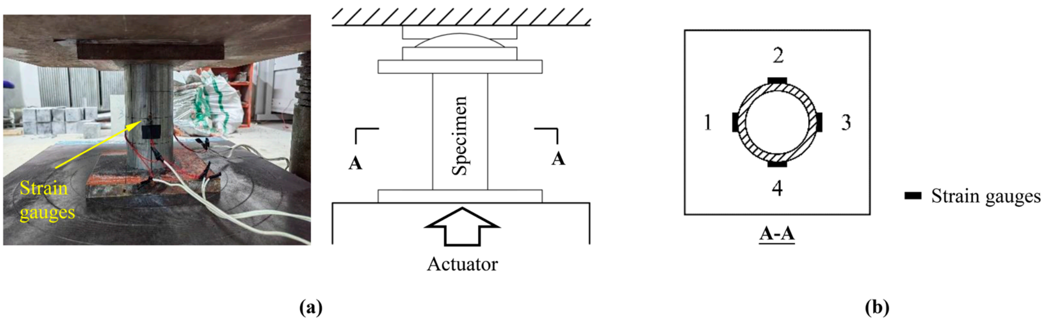

Figure 5. Stub column test arrangements: (**a**) electro-hydraulic servo testing machine; (**b**) arrangement of strain gauges.

2.4. Test Results

The load-end shortening relationship, ultimate loads (P_u), and end shortening at ultimate load (δ_u) of the stub column specimens were measured. The load-end shortening relationship is shown in Figure 6. The measured ultimate loads (P_u), end shortening at the ultimate load (δ_u), the ultimate load normalized by the cross-section yield load ($P_u/(Af_{0.2})$, where A is the gross cross-sectional area), and the failure modes of the specimens are presented in Table 4. Additionally, the cross-sectional slenderness $\overline{\lambda}_p$ in Table 4 is defined as a dimensionless parameter

$$\overline{\lambda}_p = \sqrt{f_{0.2}/\sigma_L}, \quad (2)$$

where

$$\sigma_L = \frac{E}{\sqrt{3(1-v^2)}}\frac{2t}{D}. \quad (3)$$

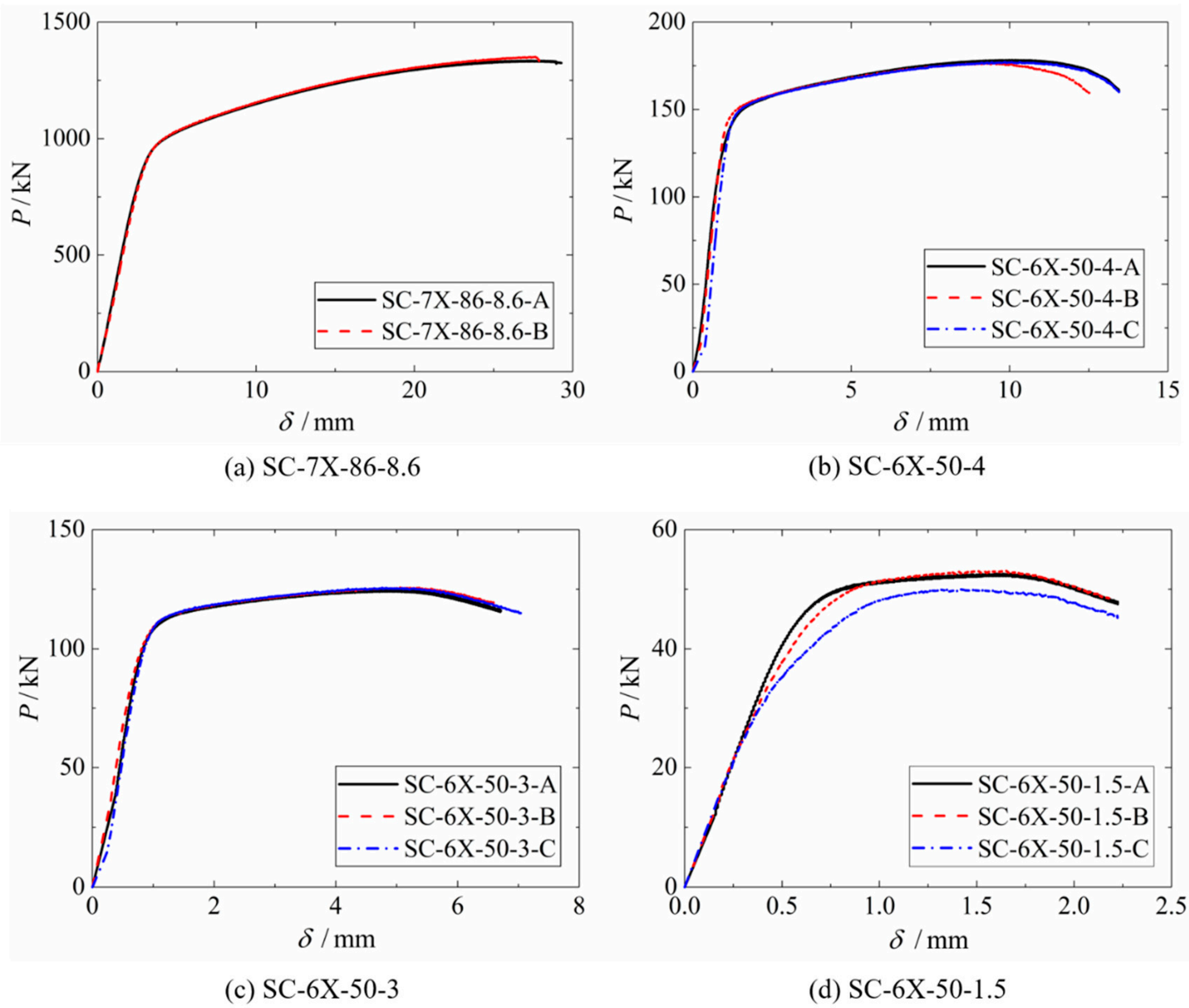

Figure 6. Load-end shortening relationship of stub columns.

Table 4. Test result of stub columns.

Specimen	$\bar{\lambda}_p$	P_u/kN	δ_u/mm	$P_u/(Af_{0.2})$	Failure Mode
SC-7X-86-8.6-A	0.229	1338	26.775	1.375	Yielding
SC-7X-86-8.6-B	0.229	1342	26.908	1.379	Yielding
SC-6X-50-4-A	0.205	178.1	9.579	1.232	Yielding
SC-6X-50-4-B	0.207	176.5	9.141	1.207	Yielding
SC-6X-50-4-C	0.212	177.1	9.495	1.201	Yielding
SC-6X-50-3-A	0.221	124.6	5.065	1.125	Yielding
SC-6X-50-3-B	0.234	126.2	5.137	1.122	Yielding
SC-6X-50-3-C	0.234	125.1	5.097	1.134	Yielding
SC-6X-50-1.5-A	0.305	52.6	1.552	1.046	Yielding
SC-6X-50-1.5-B	0.315	53.2	1.612	1.039	Yielding
SC-6X-50-1.5-C	-	50.1	1.582	-	-

As seen in Table 4, the normalized ultimate load $P_u/(Af_{0.2})$ from the test result exceeds unity (with the exception of specimen SC-6X-50-1.5-C). This suggests that the entire cross-section of the tested aluminum alloy CHS stub column yielded, and its strain hardening performance was utilized to varying degrees. The failure mode of the stub column specimen, as observed in Figure 7, is primarily manifested as elephant-foot buckling at both ends.

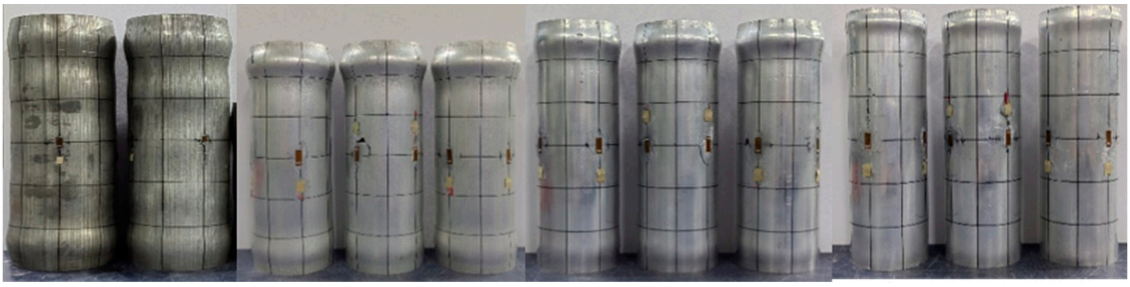

Figure 7. Failure mode of stub column specimens.

3. Numerical Modeling

3.1. FE Models

Finite element (FE) numerical models of aluminum alloy CHS stub columns are developed in this section. The primary objectives of FE modeling are twofold. Firstly, the numerical models are to accurately replicate the result of stub column tests. Subsequently, parametric studies are conducted by applying the validated FE models to extend the result to a wind range of aluminum alloy grades and diameter-to-thickness ratios.

The FE models were established using an 8-node incompatible mode solid element, C3D8I, which was shown to accurately simulate the buckling performance of aluminum alloy CHS columns in previous research [36]. The dimensions provided in Table 1 were used for the stub column modeling. As shown in Figure 8, all degrees of freedom of the section at both ends were coupled to two reference points, respectively, and were restrained except for the axial translation at the loading end. The axial load was applied via an axial displacement increment. The material is modelled with "plasticity", and true stress-plastic strain transformed via experimentally measured engineering stress-strain must be input. In the meshing scheme, the meshing size does not exceed 4 mm × 4 mm × 3 mm, and the shape should be as hexagonal as possible to ensure numerical accuracy. Linear eigenvalue analysis was initially performed to determine the buckling loads and their corresponding modes. The first-order buckling mode was introduced as an imperfection in the nonlinear buckling analysis using the Riks method, which is necessary to solve the discontinuous bifurcation problem [37,38].

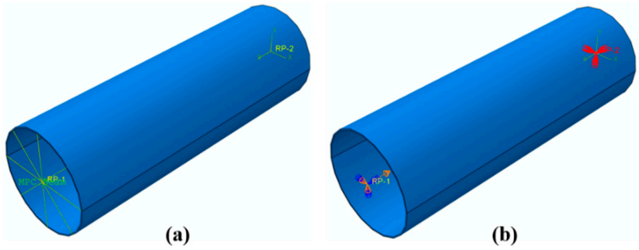

Figure 8. FE model: (**a**) MPC constraints and (**b**) boundary conditions.

3.2. Validation of FE Models

To verify the accuracy of the FE models, load-end shortening curves, ultimate loads, and failure modes generated by the FE analysis were compared with those obtained from stub column tests. The FE result of ultimate loads, $P_{u,\,FE}$, and the ratios, $P_{u,\,FE}/P_{u,\,exp}$, of the ultimate load between the FE and the test results are listed in Table 5. The mean value of $P_{u,\,FE}/P_{u,\,exp}$ is 1.006 with a corresponding COV of 0.024. A comparison between the typical failure modes of CHS stub columns obtained from the test and FE simulation is presented in Figure 9. The failure modes obtained from the FE analysis are in good agreement with the experiment. The comparison of load-end shortening curves for specimens SC-6X-50-4-B and SC-6X-50-3-C between the test and FE solutions is shown in Figure 10. As observed, the load-end shortening curve obtained via the FE analysis matches well with the test result before the peak. In conclusion, the established FE models accurately represent axial compression of aluminum alloy CHS stub columns.

Table 5. Comparison of FE and test results of CHS stub columns.

Specimen	$P_{u,\,FE}$/kN	$P_{u,\,exp}$/kN	$P_{u,\,FE}/P_{u,\,exp}$
SC-7X-86-8.6-A	1302.93	1338	0.971
SC-7X-86-8.6-B	1302.93	1342	0.971
SC-6X-50-4-A	183.628	178.1	1.031
SC-6X-50-4-B	177.805	176.5	1.007
SC-6X-50-4-C	176.080	177.1	0.994
SC-6X-50-3-A	127.225	124.6	1.021
SC-6X-50-3-B	131.708	126.2	1.044
SC-6X-50-3-C	125.527	125.8	0.998
SC-6X-50-1.5-A	53.395	52.6	1.015
SC-6X-50-1.5-B	53.644	53.2	1.008
Mean			1.006
COV			0.024

Figure 9. Comparison of failure models between test and FE solutions.

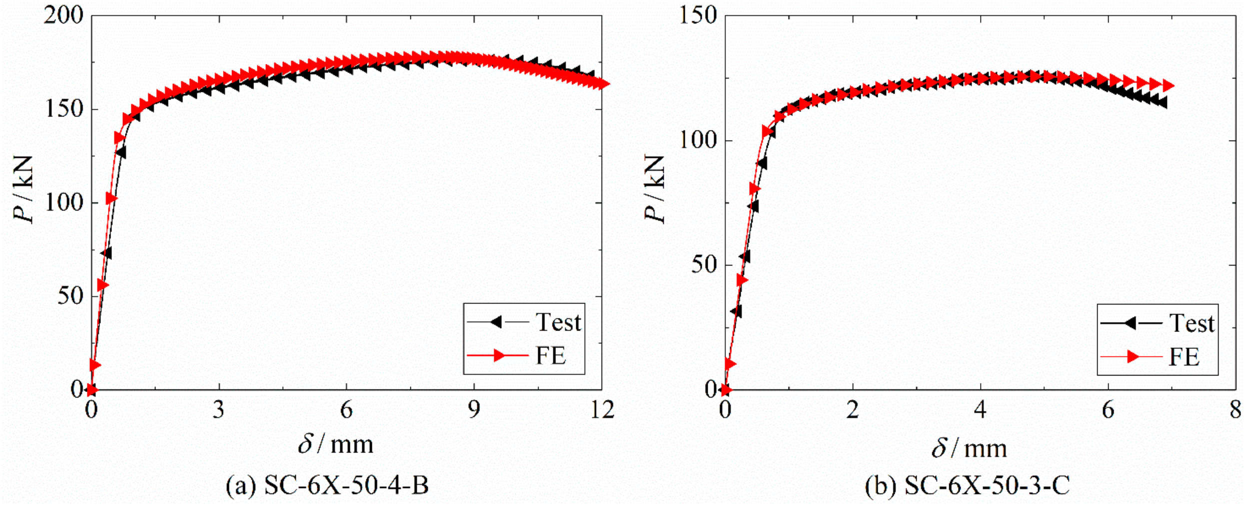

Figure 10. Comparison of load-end shortening curves between test and FE solutions: (**a**) for SC-6X-50-4-B and (**b**) for SC-6X-50-3-C.

3.3. Parametric Studies

Based on the validated FE models, a total of 125 aluminum alloy CHS stub columns were simulated considering the diversity of material properties and cross-sectional dimensions. For FE models with outer diameter-to-thickness, D/t, ratios ranging from 12.5 to 100, the length, L, is three times its outer diameter, D, to prevent overall column buckling. The range of material parameters were statistically obtained from some previous material tests as well as those in this study, including 7A04-T6, 6082-T6, 6061-T6, and 6063-T5 aluminum alloys, and are summarized as $E_1 = 63 \sim 77$ GPa, $f_{0.2} = 150 \sim 600$ MPa, $n = 0.5f_{0.2}/10 \sim 1.5f_{0.2}/10$. The design equation for aluminum alloy CHSs under axial compression combines the parametric result with the test data.

4. Establishing Prediction Formula

In this section, an accurate relation is presented for predicting the ultimate strength of high-strength aluminum alloy non-slender CHSs under axial compression by applying the CSM. Based on the experiment and FE method, the cross-section slenderness limit and base curve were optimized to enhance the accuracy of the CSM in predicting the strain hardening capacity of high-strength aluminum alloys.

4.1. Cross-Section Slenderness Limit

The maximum diameter-to-thickness ratios, known as the cross-section slenderness limits, are specified in the design codes of aluminum structures, such as EC9. Beyond these limits, strain hardening has no significant benefit due to local buckling in the compressed cross-section before yielding. The normalized cross-sectional slenderness limits ($\overline{\lambda}_s$) of the compressed cross-section stipulated in design codes were evaluated using the FE method as presented in Figure 11. Evidently, the current slenderness limits stipulated in the codes are conservative to a certain extent, and they become more conservative as yield stress increases. Therefore, further investigation is necessary to determine the cross-sectional slenderness limit of high-strength aluminum alloy CHSs under compression.

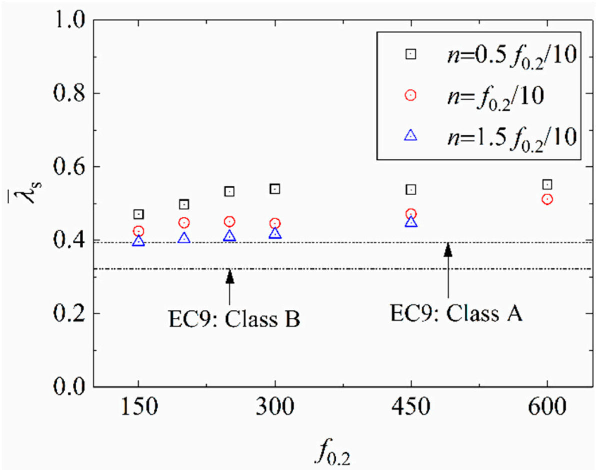

Figure 11. Comparison of FE solutions of cross-section slenderness limit with EC9.

A new cross-sectional slenderness limit is proposed in this section based on experimental data and FE solutions of high-strength aluminum alloy CHS stub columns. This limit is identified by plotting the normalized ultimate load, $P_u/(Af_{0.2})$, against normalized cross-sectional slenderness, $\bar{\lambda}_p$, as illustrated in Figure 12. Linear regression analysis was performed on a dataset comprising 26 experimental data (comprising 10 valid experimental data from Section 2 and 16 experimental data extracted from literature [39–42]) as well as 125 FE solutions. This analysis yields a normalized cross-section slenderness limit of $\bar{\lambda}_s = 0.405$.

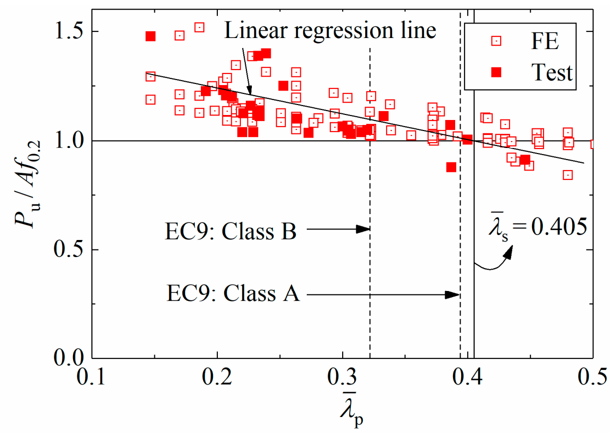

Figure 12. Normalized ultimate load $P_u/(Af_{0.2})$ varying with normalized cross-section slenderness $\bar{\lambda}_p$.

4.2. Base Curve

The base curve delineates the correlation between the deformation capacity and cross-sectional slenderness. The deformation capacity is characterized by the strain ratio, which is the normalized cross-sectional ultimate strain, ε_{csm}, divided by the yield strain, ε_y. The strain ratio, $\varepsilon_{csm}/\varepsilon_y$, for non-slender cross-sections can be determined using Equation (4) with the stub column test data,

$$\frac{\varepsilon_{csm}}{\varepsilon_y} = \frac{\varepsilon_b - 0.002}{\varepsilon_y} = \frac{\delta_u/L - 0.002}{\varepsilon_y}, \ \bar{\lambda}_p \leq \bar{\lambda}_s \quad (4)$$

where the yield strain $\varepsilon_y = f_{0.2}/E$. The base curve for non-slender cross-sections can be expressed via Equation (5). The ultimate strain (ε_{csm}) is defined with two upper bounds

($15\varepsilon_y$ and $C_1\varepsilon_u$) to constrain plastic deformation and prevent material fracture of non-slender cross-sections, as

$$\frac{\varepsilon_{csm}}{\varepsilon_y} = \frac{a}{\overline{\lambda}_p{}^b} \text{ and } \frac{\varepsilon_{csm}}{\varepsilon_y} \leq \min\left(15, \frac{C_1\varepsilon_u}{\varepsilon_y}\right), \overline{\lambda}_p \leq \overline{\lambda}_s \quad (5)$$

where a and b are constants. In a previous study [34], these constants were determined by fitting the collected compression test data of hot-finished steel, ultrahigh-strength steel, cold-formed steel, stainless steel, and normal-strength aluminum alloy CHSs. The base curve for non-slender CHSs is as follow:

$$\frac{\varepsilon_{csm}}{\varepsilon_y} = \frac{4.44 \times 10^{-3}}{\overline{\lambda}_p{}^{4.5}} \text{ and } \frac{\varepsilon_{csm}}{\varepsilon_y} \leq \min\left(15, \frac{C_1\varepsilon_u}{\varepsilon_y}\right), \overline{\lambda}_p \leq 0.3 \quad (6)$$

In this paper, the base curve for non-slender CHSs is derived by re-analyzing the test and FE result of high-strength aluminum alloy stub columns. In Figure 13, the proposed base curve in Equation (7) is illustrated, which generally serves as a lower bound for the test and FE data.

$$\frac{\varepsilon_{csm}}{\varepsilon_y} = \frac{0.045}{\overline{\lambda}_p{}^{3.437}} \text{ and } \frac{\varepsilon_{csm}}{\varepsilon_y} \leq \min\left(15, \frac{C_1\varepsilon_u}{\varepsilon_y}\right), \overline{\lambda}_p \leq 0.405 \quad (7)$$

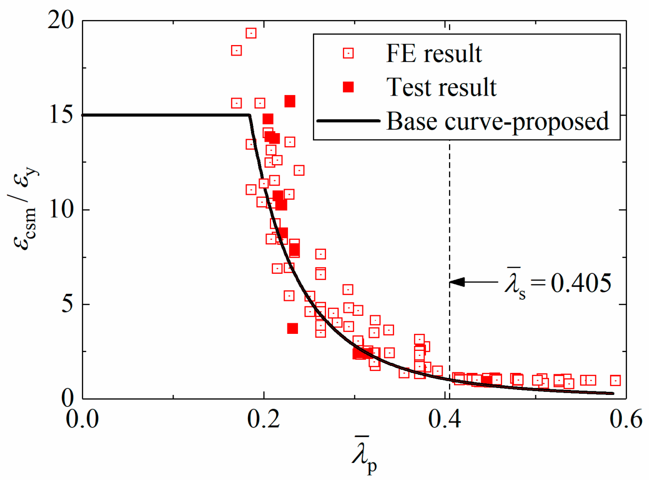

Figure 13. CSM base curve with test and FE data.

4.3. Material Models

CSM adopts an elastic, linear strain-hardening material model (i.e., a bi-linear material model) to characterize the mechanical properties of aluminum alloys, as depicted in Figure 14. The strain-hardening behavior of the material is described by the strain-hardening modulus E_{sh}:

$$E_{sh} = \frac{f_u - f_y}{C_2\varepsilon_u - \varepsilon_y}, \quad (8)$$

where the ultimate strain, ε_u, can be predicted using Equation (9), as formulated by Su et al. [25].

$$\varepsilon_u = C_3\left(1 - f_y/f_u\right) + C_4. \quad (9)$$

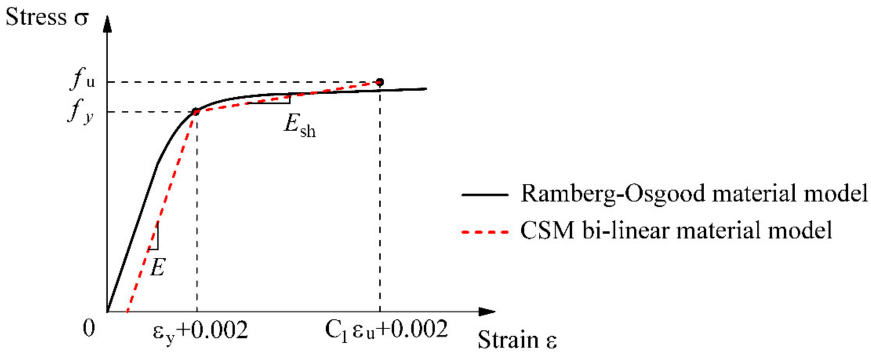

Figure 14. Elastic, linear strain-hardening material model in CSM.

The values of C_1, C_2, C_3, and C_4 for aluminum alloys are 0.5, 0.5, 0.13, and 0.06, respectively, which was proposed by Buchanan et al. [34]. The CSM limiting stress, f_{csm}, for high-strength aluminum alloy non-slender CHSs under compression is determined as follows:

$$f_{csm} = f_y + E_{sh}\varepsilon_y\left(\frac{\varepsilon_{csm}}{\varepsilon_y} - 1\right). \quad (10)$$

4.4. Cross-Sectional Capacity

The compressive capacity of high-strength aluminum alloy non-slender CHSs according to the CSM can be determined using Equation (11).

$$P_{csm} = Af_{csm}, \overline{\lambda}_p \le \overline{\lambda}_s \quad (11)$$

5. Reliability Analysis

The proposed relation for predicting the compressive bearing capacity of high-strength aluminum alloy non-slender CHSs is evaluated. The cross-sectional resistance obtained from tests ($P_{u,\,exp}$) is compared with the predicted strengths ($P_{u,\,pred}$) determined in accordance with (i) EC9, (ii) the CSM proposed by Buchanan et al. [34], and (iii) the CSM proposed in this paper. The comparison between the predicted ultimate loads normalized by the corresponding experimental data is shown in Figure 15. The mean and COV values for high-strength aluminum alloy non-slender CHSs are listed in Table 6. The mean values of $P_{u,\,exp}/P_{u,\,pred}$ obtained from EC9, Buchanan et al. [34], and the proposed equation in this paper are 1.153, 1.093, and 1.043, respectively, with corresponding COVs of 0.126, 0.062, and 0.042.

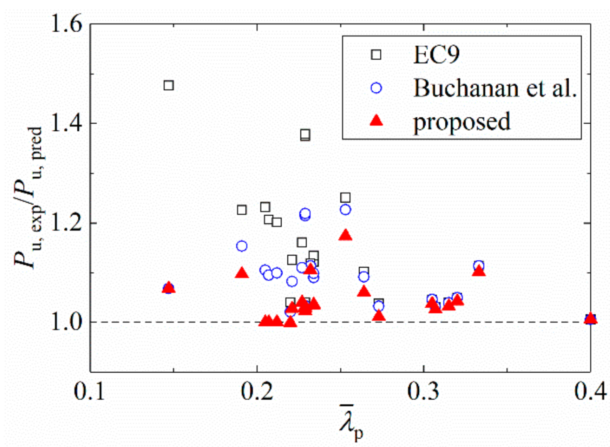

Figure 15. Comparison of test capacity of high-strength aluminum alloy CHS stub columns with predicted strength [34].

Table 6. Statistical analysis for high-strength aluminum alloy CHS stub columns.

	$P_{u, exp}/P_{u, EC9}$	$P_{u, exp}/P_{u, Buchanan}$	$P_{u, exp}/P_{u, pro}$
Mean	1.153	1.093	1.043
COV	0.126	0.062	0.042

In general and on average, the CSM can more accurately and consistently predict the cross-section compression resistance of non-slender cross-sections compared with EC9. However, the CSM prediction relation proposed by Buchanan et al. [34] is still too conservative for high-strength aluminum alloys. Considering the accuracy and consistency of compression prediction for high-strength aluminum alloy CHSs, the new CSM relation presented in this paper demonstrates an excellent result.

6. Conclusions

This paper presents experiment and numerical simulation analysis on the local buckling behavior of high-strength aluminum alloy CHSs under axial compression. Based on experiment and FE solutions, a new and improved CSM relation for predicting cross-sectional resistance of high-strength aluminum alloy CHSs is established. The main conclusions are outlined as follows:

(1) The test results indicate that 11 high-strength aluminum alloy CHS stub column specimens failed due to yielding.
(2) A FE model is established and validated using the experimental results from this paper. The agreement between the FE results and the test results in terms of cross-sectional resistance, failure modes, and load-end shortening responses is excellent.
(3) The strength prediction formula proposed by EC9, Buchanan et al. [34], and this paper are evaluated against experimental data. The comparison shows that the strength predictions from EC9 and Buchanan et al. [34] are conservative.
(4) The accuracy and consistency of the cross-sectional resistance predictions presented in this paper are significantly improved compared to the results from EC9 and Buchanan et al. [34]. The prediction formulas proposed in this paper show an 11% and 5% improvement in accuracy over EC9 and Buchanan et al. [34], respectively, while the scatter is reduced by 8.4% and 2%.

Further work is currently underway to extend the CSM for the buckling design of high-strength aluminum alloy members, as well as for FRP–aluminum alloy composite members. Utilizing the CSM to enhance the cross-sectional capacity of members will lead to lighter structures, thereby achieving more sustainable buildings.

Author Contributions: Conceptualization, L.C. and W.S.; methodology, L.C. and W.X.; software, L.C.; validation, L.C. and W.X.; data curation, Y.C.; writing—original draft preparation, L.C.; writing—review and editing, L.C., W.X. and W.S.; visualization, L.C. and Y.C.; supervision, W.S.; funding acquisition, W.S. All authors have read and agreed to the published version of the manuscript.

Funding: This research was funded by the Jilin Scientific and Technological Development Program (grant No. 20240101130JC), the Suqian Sci&Tech Program (grant No. K202346) and the Natural Science Foundation of the Jiangsu Higher Education Institutions of China (grant No. 24KJB560023).

Data Availability Statement: The original contributions presented in the study are included in the article. Further inquiries can be directed to the authors.

Conflicts of Interest: The authors declare no conflicts of interest.

References

1. Melchers, R.E. Corrosion uncertainty modelling for steel structures. *J. Constr. Steel Res.* **1999**, *52*, 3–19. [CrossRef]
2. Mazzolani, F.M. 3D aluminium structures. *Thin-Walled Struct.* **2012**, *61*, 258–266. [CrossRef]
3. Georgantzia, E.; Gkantou, M.; Kamaris, G.S. Aluminium alloys as structural material: A review of research. *Eng. Struct.* **2021**, *227*, 111372. [CrossRef]

4. Goggins, J.M.; Broderick, B.M.; Elghazouli, A.Y.; Lucas, A.S. Behaviour of tubular steel members under cyclic axial loading. *J. Constr. Steel Res.* **2006**, *62*, 121–131. [CrossRef]
5. Gusella, F.; Lavacchini, G.; Orlando, M.; Spinelli, P. Axial response of cold-formed steel bracing members with holes. *J. Constr. Steel Res.* **2019**, *161*, 70–85. [CrossRef]
6. Dutta, D. *Structures with Hollow Sections*; Wiley VCH: Weinheim, Germany, 2002.
7. *GB 50429*; Code for Design of Aluminium Structures. China Planning Press: Beijing, China, 2007.
8. *BS EN 1999-1-1*; Eurocode 9: Design of Aluminium Structures. European Committee for Standardization: Brussels, Belgium, 2007.
9. *AS/NZS 1664.1*; Australian/New Zealand Standard (AS/NZS) Aluminium Structures. Australian/New Zealand Standard: Sydney, Australia, 1997.
10. Aluminum Association. *Aluminum Design Manual*; Aluminum Association: Washington, DC, USA, 2020.
11. Yang, B.; Zhu, Q.; Nie, S.; Elchalakani, M.; Xiong, G. Experimental and model investigation on residual stresses in Q460GJ thick-walled I-shaped sections. *J. Constr. Steel Res.* **2018**, *145*, 489–503. [CrossRef]
12. Gardner, L.; Yun, X.; Walport, F. The Continuous Strength Method—Review and outlook. *Eng. Struct.* **2023**, *275*, 114924. [CrossRef]
13. Gardner, L.; Nethercot, D.A. Experiments on stainless steel hollow sections—Part 1: Material and cross-sectional behaviour. *J. Constr. Steel Res.* **2004**, *60*, 1291–1318. [CrossRef]
14. Ashraf, M.; Gardner, L.; Nethercot, D.A. Structural stainless steel design: Resistance based on deformation capacity. *J. Struct. Eng.* **2008**, *134*, 402–411. [CrossRef]
15. Gardner, L. The continuous strength method. *Proc. Inst. Civ. Eng. Struct. Build.* **2008**, *161*, 127–133. [CrossRef]
16. Liew, A.; Gardner, L. Ultimate capacity of structural steel cross-sections under compression, bending and combined loading. *Structures* **2015**, *1*, 2–11. [CrossRef]
17. Yun, X.; Gardner, L.; Boissonnade, N. The continuous strength method for the design of hot-rolled steel cross-sections. *Eng. Struct.* **2018**, *157*, 179–191. [CrossRef]
18. Yun, X.; Gardner, L.; Boissonnade, N. Ultimate capacity of I-sections under combined loading—Part 2: Parametric studies and CSM design. *J. Constr. Steel Res.* **2018**, *148*, 265–274. [CrossRef]
19. Yun, X.; Wang, Z.; Gardner, L. Structural performance and design of hot-rolled steel SHS and RHS under combined axial compression and bending. *Structures* **2020**, *27*, 1289–1298. [CrossRef]
20. Afshan, S.; Gardner, L. The continuous strength method for structural stainless steel design. *Thin-Walled Struct.* **2013**, *68*, 42–49. [CrossRef]
21. Arrayago, I.; Real, E. Experimental Study on Ferritic Stainless Steel RHS and SHS Cross-sectional Resistance Under Combined Loading. *Structures* **2015**, *4*, 69–79. [CrossRef]
22. Zhao, O.; Gardner, L. The continuous strength method for the design of mono-symmetric and asymmetric stainless steel cross-sections in bending. *J. Constr. Steel Res.* **2018**, *150*, 141–152. [CrossRef]
23. Liang, Y.; Zhao, O.; Long, Y.-L.; Gardner, L. Stainless steel channel sections under combined compression and minor axis bending—Part 2: Parametric studies and design. *J. Constr. Steel Res.* **2019**, *152*, 162–172. [CrossRef]
24. Ashraf, M.; Young, B. Compression resistance of aluminium stub columns using Continuous Strength Method. In *Tubular Structures XIII, Proceedings of the 13th International Symposium on Tubular Structures, Hong Kong, China, 15–17 December 2010*; CRC Press/Balkema: Leiden, The Netherlands, 2010; pp. 257–263.
25. Su, M.N.; Young, B.; Gardner, L. Continuous strength method for aluminium alloy structures. *Adv. Mater. Res.* **2013**, *742*, 70–75. [CrossRef]
26. Su, M.-N.; Young, B.; Gardner, L. Deformation-based design of aluminium alloy beams. *Eng. Struct.* **2014**, *80*, 339–349. [CrossRef]
27. Su, M.-N.; Young, B.; Gardner, L. Testing and design of aluminum alloy cross sections in compression. *J. Struct. Eng.* **2014**, *140*, 4014047. [CrossRef]
28. Su, M.-N.; Young, B.; Gardner, L. Continuous beams of aluminum alloy tubular cross sections. I: Tests and FE model validation. *J. Struct. Eng.* **2015**, *141*, 4014232. [CrossRef]
29. Su, M.-N.; Young, B.; Gardner, L. Continuous beams of aluminum alloy tubular cross sections. II: Parametric study and design. *J. Struct. Eng.* **2015**, *141*, 4014233. [CrossRef]
30. Lan, X.; Chen, J.; Chan, T.-M.; Young, B. The continuous strength method for the design of high strength steel tubular sections in compression. *Eng. Struct.* **2018**, *162*, 177–187. [CrossRef]
31. Lan, X.; Chen, J.; Chan, T.-M.; Young, B. The continuous strength method for the design of high strength steel tubular sections in bending. *J. Constr. Steel Res.* **2019**, *160*, 499–509. [CrossRef]
32. Zhao, O.; Gardner, L.; Young, B. Structural performance of stainless steel circular hollow sections under combined axial load and bending—Part 2: Parametric studies and design. *Thin-Walled Struct.* **2016**, *101*, 240–248. [CrossRef]
33. Zhao, O.; Rossi, B.; Gardner, L.; Young, B. Experimental and Numerical Studies of Ferritic Stainless Steel Tubular Cross Sections under Combined Compression and Bending. *J. Struct. Eng.* **2016**, *142*, 04015110. [CrossRef]
34. Buchanan, C.; Gardner, L.; Liew, A. The continuous strength method for the design of circular hollow sections. *J. Constr. Steel Res.* **2016**, *118*, 207–216. [CrossRef]
35. *GB/T 228.1*; Metallic Materials—Tensile Testing—Part 1: Method of Test at Room Temperature. China Planning Press: Beijing, China, 2010.

36. Chen, L.H.; Yu, Y.P.; Song, W.; Wang, T.W.; Sun, W.P. Stability of geometrically imperfect struts with Ramberg-Osgood constitutive law. *Thin-Walled Struct.* **2022**, *177*, 109438. [CrossRef]
37. Shen, J.; Wadee, M.A.; Sadowski, A.J. Interactive buckling in long thin-walled rectangular hollow section struts. *Int. J. Nonlin. Mech.* **2017**, *89*, 43–58. [CrossRef]
38. Bai, L.; Wadee, M.A.; Kollner, A.; Yang, J. Variational modelling of local-global mode interaction in long rectangular hollow section struts with Ramberg-Osgood type material nonlinearity. *Int. J. Mech. Sci.* **2021**, *209*, 106691. [CrossRef]
39. Zhu, J.-H.; Young, B. Experimental investigation of aluminum alloy circular hollow section columns. *Eng. Struct.* **2006**, *28*, 207–215. [CrossRef]
40. Wang, Y.; Fan, F.; Lin, S. Experimental investigation on the stability of aluminium alloy 6082 circular tubes in axial compression. *Thin-Walled Struct.* **2015**, *89*, 54–66. [CrossRef]
41. Zhou, F.; Young, B. Concrete-filled aluminum circular hollow section column tests. *Thin-Walled Struct.* **2009**, *47*, 1272–1280. [CrossRef]
42. Feng, P.; Hu, L.; Qian, P.; Ye, L. Compressive bearing capacity of CFRP-aluminum alloy hybrid tubes. *Compos. Struct.* **2016**, *140*, 749–757. [CrossRef]